SLC-30A9 is required for Zn^{2+} homeostasis, Zn^{2+} mobilization, and mitochondrial health

Huichao Deng[a,b,1], Xinhua Qiao[a,1], Ting Xie[a,c], Wenfeng Fu[a,b], Hang Li[a,b], Yanmei Zhao[d], Miaomiao Guo[a,b], Yaqian Feng[e], Ligong Chen[e], Yan Zhao[a], Long Miao[b,d], Chang Chen[a,b,2], Kang Shen[f,g,2], and Xiangming Wang[a,2]

[a]National Laboratory of Biomacromolecules, Chinese Academy of Sciences Center for Excellence in Biomacromolecules, Institute of Biophysics, Chinese Academy of Sciences, Beijing 100101, China; [b]College of Life Sciences, University of Chinese Academy of Sciences, Beijing 100049, China; [c]School of Basic Medical Sciences, Southwest Medical University, Luzhou 646000, China; [d]Key Laboratory of RNA Biology, Chinese Academy of Sciences Center for Excellence in Biomacromolecules, Institute of Biophysics, Chinese Academy of Sciences, Beijing 100101, China; [e]School of Pharmaceutical Sciences, Key Laboratory of Bioorganic Phosphorus Chemistry and Chemical Biology (Ministry of Education), Tsinghua University, Beijing 100084, China; [f]HHMI, Stanford University, Stanford, CA 94305; and [g]Department of Biology, Stanford University, Stanford, CA 94305

The trace element zinc is essential for many aspects of physiology. The mitochondrion is a major Zn^{2+} store, and excessive mitochondrial Zn^{2+} is linked to neurodegeneration. How mitochondria maintain their Zn^{2+} homeostasis is unknown. Here, we find that the SLC-30A9 transporter localizes on mitochondria and is required for export of Zn^{2+} from mitochondria in both *Caenorhabditis elegans* and human cells. Loss of *slc-30a9* leads to elevated Zn^{2+} levels in mitochondria, a severely swollen mitochondrial matrix in many tissues, compromised mitochondrial metabolic function, reductive stress, and induction of the mitochondrial stress response. SLC-30A9 is also essential for organismal fertility and sperm activation in *C. elegans*, during which Zn^{2+} exits from mitochondria and acts as an activation signal. In *slc-30a9*–deficient neurons, misshapen mitochondria show reduced distribution in axons and dendrites, providing a potential mechanism for the Birk–Landau–Perez cerebrorenal syndrome where an *SLC30A9* mutation was found.

Zn^{2+} transporters | SLC-30A9 | mitochondria | Birk–Landau–Perez cerebrorenal syndrome

Zinc is the second most abundant trace element (after iron) and plays important roles in numerous cellular functions (1). It serves as a structural component for many proteins such as transcription factors and numerous enzymes including oxidoreductase and alcohol dehydrogenase (1). Deficiency or excess of Zn^{2+} due to disruption of Zn^{2+} homeostasis leads to a wide range of disease conditions (2). Zn^{2+} concentration at various cellular compartments is regulated to achieve the appropriate levels at steady state. It is also suggested that Zn^{2+} might function as a neuromodulator (3) and second messenger (4). Therefore, dynamic regulation of Zn^{2+} levels across cellular compartments likely contributes to normal physiology.

Two families of transporters, SLC-30 (ZnT; zinc transporter) and SLC-39 (ZIP; zinc–iron permease), are key regulators of cellular Zn^{2+} (5). They function in opposite directions to maintain Zn^{2+} homeostasis (6). Each ZnT family protein contains six transmembrane domains and lowers cytoplasmic Zn^{2+} by transporting Zn^{2+} into intracellular organelles or to the extracellular space when cellular Zn^{2+} level is high. On the contrary, each ZIP family protein contains eight transmembrane domains and functions to elevate cytoplasmic Zn^{2+} by exporting Zn^{2+} from various organelles or importing Zn^{2+} from the extracellular space when cytosolic Zn^{2+} is low (7). Ten ZnTs (*SI Appendix*, Fig. S1*A*) and 14 ZIP transporters with different organelle localization are encoded by the human genome. For example, SLC-30A2, ZIP3, and ZIP8 localize to the lysosome membrane. SLC-30A5, SLC-30A6, SLC-30A7, ZIP9, and ZIP13 are targeted to the Golgi apparatus (6, 7).

Mitochondrial uptake of Zn^{2+} provides a clearance mechanism for cytosolic Zn^{2+}, especially in neurons under excitotoxicity conditions (8). Excessive mitochondrial Zn^{2+} is correlated with reduced mitochondrial membrane potential, increased production of reactive oxygen species, and ultimately neuronal cell death (9). However, little is known about how mitochondrial Zn^{2+} is regulated. SLC-39A8 is localized on mitochondria and perturbation of SLC-39A8 using a short interfering RNA impairs mitochondrial function (10). However, direct transporter function of SLC-39A8 was not tested. Zn^{2+} can enter mitochondria through the mitochondrial calcium uniporter (MCU) to cause swollen mitochondria under ischemic conditions (11, 12). However, MCU-independent transport mechanisms have also been reported (13). Therefore, definitive identification of Zn^{2+} transporters on mitochondria is necessary to understand mitochondrial physiology under normal and disease conditions.

Zinc is essential for sperm activity in many animal species (6, 14, 15). In mice, a unique subcellular Zn^{2+} distribution is associated with sperm capacitation (16). Intracellular Zn^{2+} mobilization and release to the extracellular matrix have also been linked to sperm activation in *Caenorhabditis elegans* (6). *C. elegans* sperm can be activated by several factors, including the weak base triethanolamine (TEA), ammonium chloride, and Pronase in vitro, and through

Significance

Zinc plays important roles in numerous cellular processes. Deficiency or excess of Zn^{2+} leads to many diseases. Zn^{2+} concentration at various cellular compartments is regulated. Imbalance of Zn^{2+} in mitochondria has been linked to neurodegeneration. However, little is known about how mitochondrial Zn^{2+} is regulated. We find that SLC-30A9 is required for Zn^{2+} export from mitochondria in both *Caenorhabditis elegans* and human cells. Loss of *slc-30a9* leads to excessive Zn^{2+} accumulation in mitochondria, severe mitochondrial swelling, compromised mitochondrial metabolic function, reductive stress, and induction of the mitochondrial stress response. SLC-30A9 is also essential for organismal fertility and sperm activation. In neurons, *slc-30a9* mutations cause dramatically reduced mitochondria in neurites, providing a potential mechanism for the Birk–Landau–Perez cerebrorenal syndrome.

SPE-8–dependent and –independent pathways in vivo (17). Extracellular Zn^{2+} modulates sperm activation through the SPE-8 pathway (6). A critical step in the sperm activation process is fusion of specialized lysosomes, membranous organelles (MOs), with the plasma membrane which leads to secretion of MO components required for sperm motility and fertilization (18). Sperm activation in worms is also accompanied by morphological changes driven by the dynamics of the cytoskeleton composed of major sperm proteins (17). SLC-39A7/ZIPT-7.1, a member of the SLC-39 family and putative Zn^{2+} transporter, is required for sperm activation (19). However, the exact mechanism of how Zn^{2+} is mobilized in sperm during the activation process remains elusive.

Here, we show that a member of the SLC-30 family, SLC-30A9, exports Zn^{2+} from mitochondria. In the *slc-30a9* mutant, mitochondria in multiple tissues become swollen and accumulate excessive Zn^{2+} in both worm and human cells. Ultrastructural experiments show that the mutant mitochondria are enlarged, with disappearing cristae in both worm sperm and HeLa cells. SLC-30A9 is required for sperm activation by the weak base TEA/ammonium chloride, during which Zn^{2+} is extruded from mitochondria. Zn^{2+} chelators and a mitochondrial membrane potential blocker hamper sperm activation, further supporting the model that SLC-30A9 mediates proton gradient–dependent Zn^{2+} mobilization from mitochondria. We also report that *SLC30A9*–knockout (KO) cells exhibit a multitude of mitochondrial functional defects.

Results

Mitochondria Are Swollen in the *slc-30a9* Mutant. To understand the molecular mechanisms that maintain mitochondrial morphology and distribution in neurons, we labeled mitochondria using the outer-membrane protein TOMM-20(1-54AA) fused with green fluorescent protein (GFP) in the *C. elegans* sensory neuron PVD and performed a forward genetic screen based on the TOMM-20::GFP signal. In wild-type (WT) animals, mitochondria were densely distributed within the cell body, displaying a small vesicle-like appearance in SIM (structure illumination microscopy) images (Fig. 1*A*). We isolated a mutant, *wy50572*, with dramatically swollen mitochondria in the PVD cell body, where the mitochondria displayed a "clusters of grapes" appearance with an enlarged vesicle lumen (Fig. 1 *A* and *B*). Using snip–single-nucleotide polymorphism mapping and next-generation sequencing, we identified a splice-site mutation in the *slc-30a9* gene, which caused a premature stop codon (*SI Appendix*, Fig. S1*B*). To verify that the *slc-30a9* mutation causes mitochondrial phenotypes, we generated a frameshift deletion in the second exon of *slc-30a9(wy50591)* using CRISPR-Cas9 (*SI Appendix*, Fig. S1*B*). Both alleles exhibited an indistinguishable swollen mitochondrial phenotype in the PVD cell body (Fig. 1 *A* and *B*), suggesting *slc-30a9* mutations are responsible for the phenotype. Expression of WT SLC-30A9 using a PVD promoter fully rescued the *slc-30a9* mutation phenotype (Fig. 1 *A* and *B*), indicating that *slc-30a9* regulates mitochondrial morphology in a cell-autonomous manner.

To test if *slc-30a9* also functions in other tissues besides neurons, we examined mitochondrial markers in muscle (GFP::MIRO-1) and epidermis (TOMM-20::mCherry). We found fully penetrant, markedly swollen mitochondria in both muscle and epidermis (Fig. 1*C*), indicating *slc-30a9* is required in multiple worm tissues to maintain mitochondrial morphology.

To further understand the mitochondrial morphology defect of the *slc-30a9* mutant, we performed electron microscopy (EM) to visualize mitochondria in *C. elegans* sperm. In control sperm (*him-5* mutants), the mitochondria were round in cross-sections with clear cristae. The average diameter of mitochondria in the EM sections was about 500 nm (Fig. 1 *D* and *E*). In contrast, the mitochondrial diameter in the *slc-30a9* mutant nearly doubled with greatly reduced cristae (Fig. 1 *D* and *E*). The disappearing cristae and increased diameter suggest that the mitochondrial swelling is due to an expanded matrix. As controls, we also compared

the morphology of the lysosome (NUC-1::mCherry) and endoplasmic reticulum (ER) (GFP::TRAM-1) in epidermis between the WT and *slc-30a9* mutant, and found no significant differences between the two genotypes (*SI Appendix*, Fig. S1 *C* and *D*), suggesting that the mitochondrial defect might be specific.

To understand the subcellular localization of SLC-30A9, we fused GFP to the C terminus of SLC-30A9 and expressed it in PVD. This construct fully rescued the *slc-30a9* mutant phenotype (Fig. 1 *A* and *B*), indicating that the fusion construct is functional. SLC-30A9::GFP showed near-complete colocalization with a mitochondrial marker, TOMM-20::mCherry, in both the PVD neuron and epidermis, indicating that SLC-30A9 mainly localizes to mitochondria (Fig. 1 *F* and *G*), which is consistent with the specific mitochondrial defects in the *slc-30a9* mutant.

SLC30A9 Is Required for Maintaining Mitochondrial Morphology in Human Cells. To test if the function of SLC30A9 is conserved in vertebrate systems, we first expressed human SLC30A9 fused to GFP (SLC30A9-GFP) together with a mitochondria-localized peptide fused to mKate (mito-mKate) in HeLa cells. We found near-perfect colocalization between the two proteins, suggesting that SLC30A9 is localized on mitochondria in vertebrate cells (Fig. 2*A*).

To investigate the function of SLC30A9, we used CRISPR-Cas9 to generate a *SLC30A9*–KO human HeLa cell line (*SLC30A9$^{-/-}$*). We also generated a HeLa cell line that stably expressed Cas9 and mCherry as a control (WT). The knockout line was confirmed by sequencing, qPCR, and Western blot (*SI Appendix*, Fig. S2 *A–C*). Furthermore, we used an antibody against SLC30A9 to visualize endogenous SLC30A9 in WT and *SLC30A9$^{-/-}$* HeLa cells, and found the SLC30A9 immunofluorescence was colocalized with the mitochondrial signal in WT HeLa cells, supporting that SLC30A9 localizes to mitochondria. We also observed dim signal outside mitochondria, suggesting minor SLC30A9 might localize on a nonmitochondrial region. Furthermore, the SLC30A9–KO cells also presented some background, suggesting the antibody we used might recognize other proteins (*SI Appendix*, Fig. S2*D*).

Consistent with the results from *C. elegans*, mitochondrial morphology was altered in *SLC30A9$^{-/-}$* cells when visualized by MitoTracker blue. While WT HeLa cells showed string-like mitochondria, *SLC30A9$^{-/-}$* cells showed vesicle-like mitochondria with their lumen visible under light microscopy (Fig. 2 *B* and *C*), suggesting that the mitochondria are swollen. One point mutation in human SLC30A9(A350Del) was found in patients with a cerebrorenal syndrome (20). To test if this mutation affects the function of SLC30A9, we transfected the *SLC30A9$^{-/-}$* HeLa cells with SLC30A9-GFP or a SLC30A9(A350Del)-GFP construct by lentivirus transduction, and the percentage of swollen mitochondria was counted. The rescue percentage in the SLC30A9-A350Del group was significantly lower than in the SLC30A9 WT group (Fig. 2 *B* and *C*), indicating that the disease allele of SLC30A9-A350Del represents loss of function. We also used transmission electron microscopy (TEM) to characterize the ultrastructural feature of mitochondrial morphology. While WT mitochondria showed a typical rod-like morphology with parallel cristae, *SLC30A9$^{-/-}$* cells exhibited ball-like mitochondria with an enlarged matrix and reduced and disorganized cristae (Fig. 2*D*). Together, these results show that SLC30A9 localizes to mitochondria and its role in maintaining mitochondrial morphology is evolutionarily conserved.

SLC-30A9 Functions on Mitochondria to Export Zinc. SLC-30A9 is predicted to be a Zn^{2+} transporter and share extensive sequence homology with the bacterial Zn^{2+}/H^+ exchanger YiiP (21). To test if SLC-30A9 functions as a Zn^{2+}/H^+ exchanger to regulate mitochondrial morphology, we used sequence homology and the known protein structures of YiiP, ZnT2, and ZnT8 to predict the Zn^{2+}/H^+ binding sites (*SI Appendix*, Fig. S3*A*). We introduced the D323A and H198A mutations to disrupt the putative Zn^{2+}/H^+ binding sites (22–24). The H198A variant partially rescued the mitochondrial
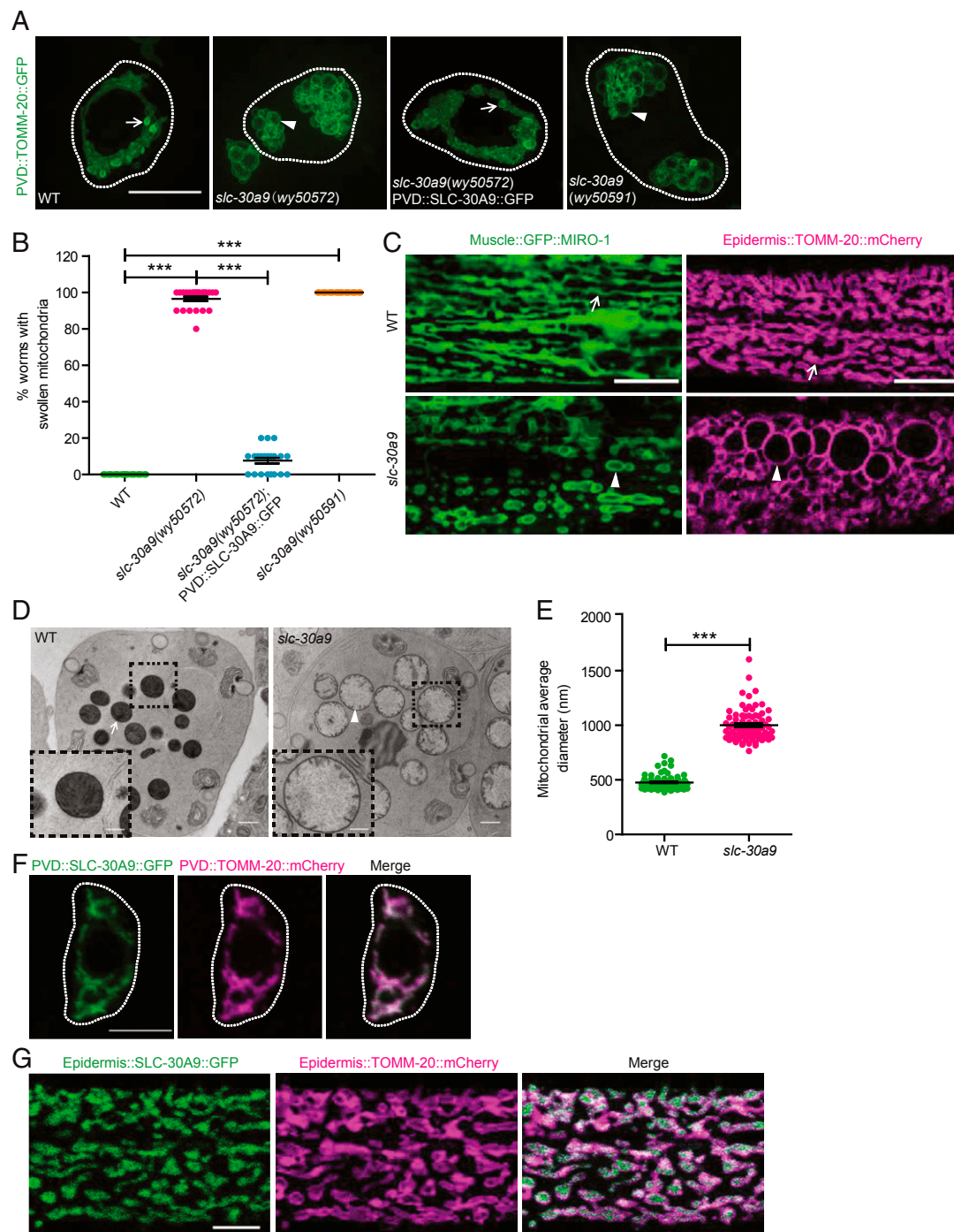
Fig. 1. Mitochondria show swollen morphology in the *slc-30a9* mutant. (*A*) Representative SIM images showing mitochondrial pattern and morphology in PVD soma in various genotypes, visualized by *ser-2*Prom3::TOMM-20(1-54AA)::GFP. Dotted white lines mark the outline of the PVD soma. The arrows point to typical normal mitochondrial morphology, and the arrowheads indicate swollen mitochondria with an enlarged lumen. (Scale bar, 5 μm.) (*B*) Quantification of the swollen mitochondrial phenotype of the WT, *wy50572*, and *wy50572* with SLC-30A9::GFP rescuing the transgene and *wy50591* mutant. Data are shown as mean ± SEM. One-way ANOVA with Tukey correction. ***$P < 0.001$. Two hundred worms or more were scored for each genotype. (*C*) Representative confocal images showing mitochondrial morphology in *C. elegans* muscle (labeled by muscle::GFP::MIRO-1) and epidermis (labeled by epidermis::TOMM-20::mCherry) in the WT and *slc-30a9*(*wy50591*). The arrows point to typical normal mitochondria, and the arrowheads indicate swollen mitochondria with an enlarged lumen. (Scale bars, 10 μm.) (*D*) TEM images of *C. elegans* sperm of *him-5*(*e1490*) and *slc-30a9*(*wy50591*); *him-5*(*e1490*). (Scale bars, 500 nm.) (*D, Insets*) Magnified views of the boxed regions. (Scale bars, 200 nm.) The arrow shows a typical mitochondrion, and the arrowhead indicates a swollen mitochondrion. (*E*) Quantification of the mitochondrial diameter of sperm in *him-5*(*e1490*) and *slc-30a9*(*wy50591*); *him-5*(*e1490*). Data are shown as mean ± SEM. ***$P < 0.001$ by unpaired *t* test. Seventy-nine or more mitochondria were analyzed for each genotype. (*F*) Representative confocal images of PVD soma coexpressing TOMM-20(1-54AA)::mCherry and SLC-30A9::GFP. Dotted white lines mark the outline of PVD soma. (Scale bar, 5 μm.) (*G*) Representative confocal images of an epidermis cell coexpressing TOMM-20(1-54AA)::mCherry and SLC-30A9::GFP. (Scale bar, 5 μm.)
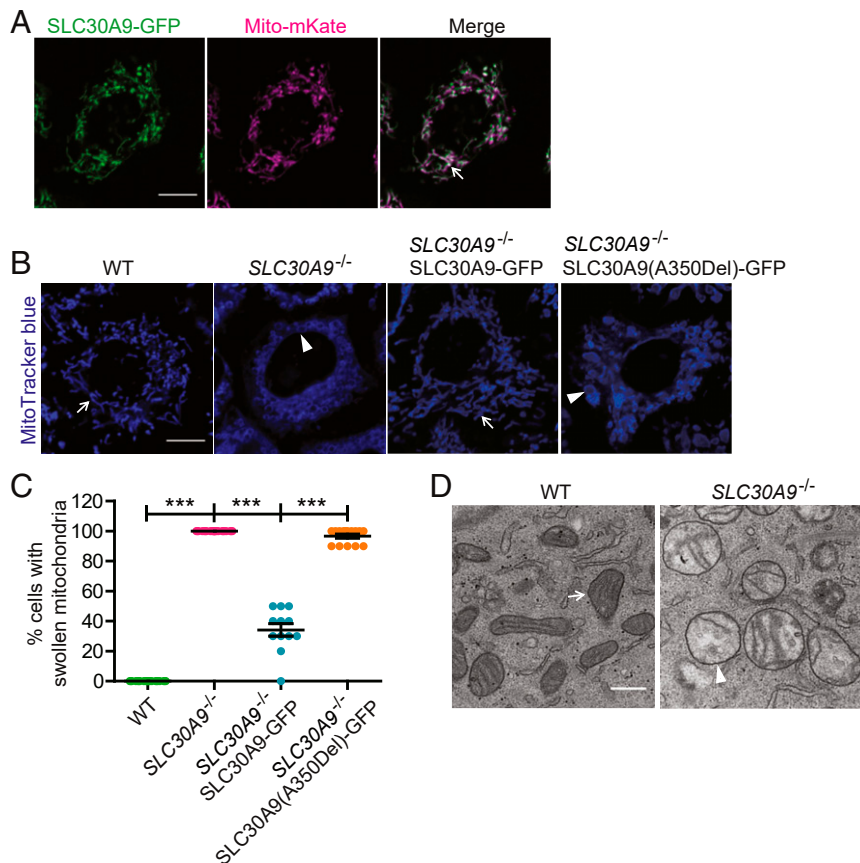
Fig. 2. Mitochondria show a swollen morphology in SLC30A9–deficient HeLa cells. (*A*) Representative confocal images of a HeLa cell coexpressing mitochondria-mKate and SLC30A9-GFP. The arrow indicates mitochondria. (Scale bar, 10 μm.) (*B*) Representative confocal images showing mitochondrial pattern and morphology, visualized by MitoTracker blue in HeLa WT, *SLC30A9*$^{-/-}$, *SLC30A9*$^{-/-}$ SLC30A9-GFP, and *SLC30A9*$^{-/-}$ SLC30A9(A350Del)-GFP cells. The arrows show typical normal mitochondria, and the arrowheads indicate swollen mitochondria. (Scale bar, 10 μm.) (*C*) Quantification of the swollen mitochondrial phenotype of HeLa WT, *SLC30A9*$^{-/-}$, *SLC30A9*$^{-/-}$ SLC30A9-GFP, and *SLC30A9*$^{-/-}$ SLC30A9(A350Del)-GFP cells. Data are shown as mean ± SEM. One-way ANOVA with Tukey correction. ***$P < 0.001$. One hundred and fifty cells or more were scored for each genotype. (*D*) TEM images of mitochondria in WT and *SLC30A9*$^{-/-}$ HeLa cells. (Scale bar, 500 nm.) The arrow points to a normal mitochondrion, and the arrowhead indicates a swollen mitochondrion.

swelling phenotype of *slc-30a9*, while the D323A variant showed no rescuing activity (Fig. 3 *A* and *B*). These results suggest that SLC-30A9 likely utilizes the mitochondrial proton gradient to transport Zn^{2+}.

To directly test this idea, we expressed the mitochondria-localized, genetically encoded Zn^{2+} sensor Mito-ZapCY1 in PVD (25). Mito-ZapCY1 colocalizes with the mitochondrial marker PVD::TOMM-20::mCherry in the cell body (*SI Appendix*, Fig. S3*B*). Mito-ZapCY1 is a sensor based on fluorescence resonance energy transfer (FRET). To measure FRET efficiency, we compared the cyan fluorescent protein (CFP) intensity before and after bleaching citrine. We found that the FRET efficiency in the *slc-30a9* mutant is significantly higher than that in the WT, indicative of an abnormally high level of mitochondrial Zn^{2+} in the *slc-30a9* mutant (*SI Appendix*, Fig. S3*C*). To verify this result, we used the chemical Zn^{2+} indicator Zinpyr-1 to stain isolated *C. elegans* spermatids. Zinpyr-1 fluorescence showed extensive colocalization with that of MitoTracker, suggesting that the mitochondria are one of the major Zn^{2+} stores in spermatids (Fig. 3*C*). Interestingly, when we performed the same experiments in the *slc-30a9* mutant spermatids, the Zinpyr-1 fluorescence intensity was dramatically higher in mitochondria of the mutant, further supporting the notion that SLC-30A9 extrudes Zn^{2+} from mitochondria (Fig. 3 *C* and *D*). Furthermore, the zinc chelator TPEN (*N,N,N′,N′*-tetrakis[2-pyridylmethyl]ethylenediamine) could reduce mitochondrial Zinpyr-1 fluorescence intensity in the *slc-30a9* mutant spermatids (Fig. 3 *C* and *D*). As controls, we

compared the Zn^{2+} level in the ER using an ER-targeted Zn^{2+} indicator (ER-ZapCY1) between the WT and *slc-30a9* mutant, and found no significant differences in FRET efficiency between the two genotypes (*SI Appendix*, Fig. S3 *D* and *E*). We also compared the nuclear Zn^{2+} level between WT and *SLC30A9*$^{-/-}$ HeLa cells, and found no significant differences in Zinpyr-1 fluorescence intensity in the nucleus between the two genotypes (*SI Appendix*, Fig. S3 *F* and *G*). These results suggest that SLC-30A9 mainly functions on mitochondria.

In HeLa cells, the Zinpyr-1 staining pattern also closely matched that of MitoTracker, indicating that mitochondria also serve as one of the major Zn^{2+} stores in vertebrate cells, consistent with a previous report (26). When compared with WT controls, the mitochondrial Zn^{2+} level in *SLC30A9*$^{-/-}$ cells was also significantly increased, agreeing with the results from *C. elegans* neurons and sperm (Fig. 3 *E* and *F*).

Taken together, these results argue that SLC30A9 is a conserved, putative Zn^{2+} transporter on mitochondria. It functions to lower mitochondrial Zn^{2+}, possibly through a Zn^{2+}/H^+ exchange mechanism.

Mitochondrial Functions Are Defective in *SLC30A9*$^{-/-}$ Cells. To investigate whether SLC30A9 is required for mitochondrial function, we measured the oxygen consumption rates (OCRs) in WT and *SLC30A9*$^{-/-}$ HeLa cells using a metabolic analyzer. We treated the cells sequentially with oligomycin, the decoupler carbonyl cyanide
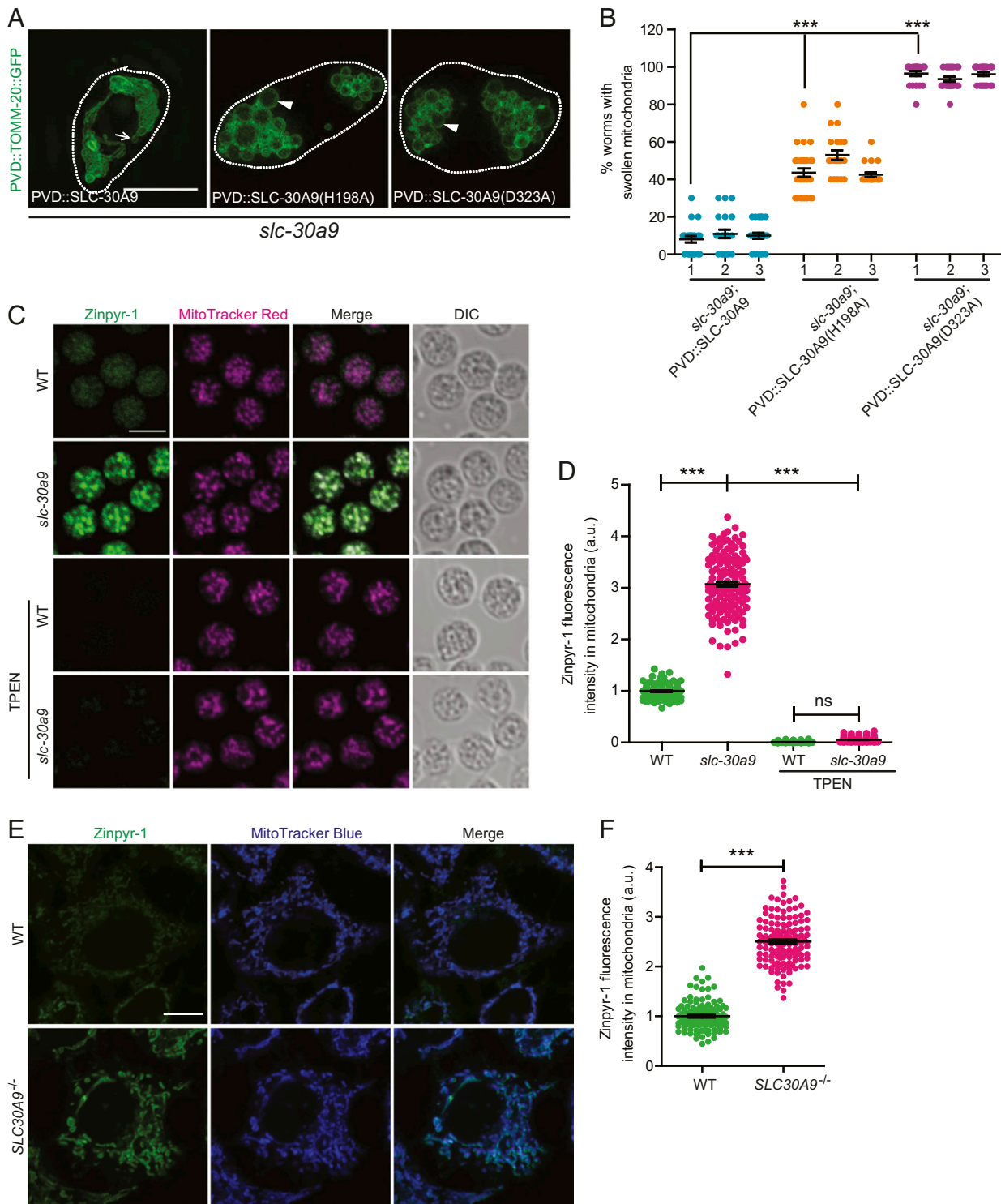
Fig. 3. SLC-30A9 exports Zn^{2+} out of mitochondria. (*A*) Representative SIM images showing mitochondrial morphology, visualized by *ser*-2Prom3::TOMM-20(1-54AA)::GFP in PVD cell soma of *slc-30a9*(*wy50572*) mutant worms expressing PVD::SLC-30A9, PVD::SLC-30A9(H198A), or PVD::SLC-30A9(D323A). Dotted white lines mark the profile of PVD soma. The arrow indicates a typical normal mitochondrion, and the arrowheads indicate swollen mitochondria with an enlarged lumen. (Scale bar, 5 μm.) (*B*) Quantification of worms with swollen mitochondria in *slc-30a9*(*wy50572*) mutant animals expressing different rescuing constructs. Three independent transgenic lines were quantified for each construct. Data are shown as mean ± SEM. One-way ANOVA with Tukey correction. ***$P < 0.001$. Two hundred worms or more were scored for each genotype. (*C*) Representative confocal images of spermatids costained with Zinpyr-1 and MitoTracker red supplemented with the zinc chelator TPEN. (Scale bar, 5 μm.) DIC, differential interference contrast. (*D*) Quantification of Zinpyr-1 fluorescence intensity in the sperm mitochondria of *him-5*(*e1490*) and *slc-30a9*(*wy50591*); *him-5*(*e1490*) and supplemented with the zinc chelator TPEN. Data are shown as mean ± SEM. One-way ANOVA with Tukey correction. ***$P < 0.001$; ns, not significant. One hundred sperm or more were scored for each genotype. a.u., arbitrary unit. (*E*) Representative confocal images of WT or *SLC30A9*$^{-/-}$ HeLa cells costained with Zinpyr-1 and MitoTracker blue. (Scale bar, 10 μm.) (*F*) Quantification of mitochondrial Zinpyr-1 fluorescence intensity in the WT and *SLC30A9*$^{-/-}$. Data are shown as mean ± SEM. ***$P < 0.001$ by unpaired *t* test. More than 119 cells were analyzed for each genotype.

4-(trifluoromethoxy) phenylhydrazone (FCCP), and a mixture of rotenone and antimycin A to calculate the adenosine triphosphate (ATP)–linked OCR and the maximal respiration capacity (27). Both parameters were significantly lower in the $SLC30A9^{-/-}$ cells compared with those of the WT controls (Fig. 4 A and B), indicating that metabolic activity is defective in $SLC30A9^{-/-}$ cells. To verify this result, we used Mito-SoNar to detect the level of NADH/NAD$^+$ in situ. Mito-SoNar is a highly sensitive NADH/NAD$^+$–specific sensor with subcellular resolution (28). As a positive control, we treated cells with pyruvate and indeed observed that the 420/485–nm ratio was increased after the treatment (*SI Appendix*, Fig. S4 *A* and *B*). The steady-state NADH/NAD$^+$ ratio in $SLC30A9^{-/-}$ cells was significantly lower than the controls, consistent with the notion that OCR is reduced in the mutant cells (Fig. 4C).

To further explore the mechanisms responsible for the reduced cellular OCR in $SLC30A9^{-/-}$ cells, we first measured the abundance of mitochondrial respiratory complexes using OXPHOS antibodies. We found that the complex I subunit NDUFB8 and the complex III subunit UQCRC2 were reduced, while the V-ATP5A level was normal in the mutant cells (Fig. 4 D and E). We next directly measured the activity of mitochondrial respiratory chain complex I and found that it was lower in the $SLC30A9^{-/-}$ cells (Fig. 4F). To measure the cellular redox, we used a mitochondria-targeted Grx1-roGFP2 construct to read out the ratio between reduced glutathione (GSH) and oxidized glutathione (GSSG) (29). Dithiothreitol and diamide treatment of Mito-Grx1-roGFP2–transfected HeLa cells caused the GSH/GSSG ratio to increase and decrease, respectively, confirming this sensor as a redox indicator (*SI Appendix*, Fig. S4 *C* and *D*). Compared with controls, $SLC30A9^{-/-}$ cells showed a significantly increased GSH/GSSG ratio, indicating that mutant mitochondria are abnormally reductive (Fig. 4G). To further verify this point, we extracted mitochondria from HeLa cells and tested the GSH/GSSG ratio using a GSH/GSSG assay kit. The data were consistent with the redox indicator in that $SLC30A9^{-/-}$ mitochondria showed a significantly increased GSH/GSSG ratio (Fig. 4H). Therefore, the high GSH/GSSG ratio in the $SLC30A9^{-/-}$ cells is consistent with decreased oxidation and mitochondrial inactivity. Taken together, these data suggest that Zn^{2+} imbalance across the mitochondrial membranes combined with morphological defects likely causes defective oxidative phosphorylation and compromised mitochondrial functions.

Mitochondrial Stress Response Is Activated in the *slc-30a9* Mutant. Given the dramatically swollen mitochondria and multiple mitochondrial functional defects, we next asked if the mitochondrial stress response is induced in the *slc-30a9* mutant. We measured the intensity of P*hsp-6*::GFP, a mitochondrial chaperone which is essential for the mitochondrial unfolded protein response (UPRmt). P*hsp-6*::GFP showed a dim signal in the WT but the expression was dramatically enhanced in the *slc-30a9* mutant (Fig. 4 *I* and *J*), indicating that Zn^{2+} overload in mitochondria might trigger UPRmt. In contrast, the ER unfolded protein response (UPRer), measured by the ER chaperone P*hsp-4*::GFP, was indistinguishable between the WT and *slc-30a9* mutant (Fig. 4 *K* and *L*), indicating UPRer is not induced in the *slc-30a9* mutant. Together, these results suggest that Zn^{2+} imbalance leads to a UPRmt.

SLC-30A9 Is Required for Sperm Activation. Next, we investigated the physiological function of mitochondrial Zn^{2+} regulation by SLC-30A9. First, we investigated sperm activation by comparing WT and *slc-30a9* mutant sperm. WT sperm developed pseudopods when treated with the sperm activator TEA (Fig. 5A) (18). TEA treatment also caused a rapid decrease of Zinpyr-1 intensity from mitochondria and an increase of intensity in the lysosome-like MO, indicative of Zn^{2+} mobilization from mitochondria to MOs (Fig. 5A). This is consistent with the existing literature, which also suggests that MOs will subsequently fuse with the plasma membrane and secrete its contents (6). In contrast, *slc-30a9* mutant

spermatids rarely formed pseudopods, demonstrating that SLC-30A9 is required for TEA-induced sperm activation (Fig. 5A). Coincidently, TEA-induced Zn^{2+} mobilization was also greatly impaired in mutant sperm, in which Zn^{2+} failed to exit from and remained high in the mitochondria (Fig. 5 A and B). Interestingly, extracellular addition of Zn^{2+} induced pseudopod formation in *slc-30a9* mutant sperm, suggesting that SLC-30A9–mediated Zn^{2+} mobilization from mitochondria to the extracellular space activates sperm (Fig. 5 C and D).

Because putative Zn^{2+}/H$^+$ binding sites of SLC-30A9 are required for its rescuing activity, we hypothesized that the mitochondrial H$^+$ gradient is required for SLC-30A9–mediated Zn^{2+} extrusion. To test this idea, we treated sperm with CCCP (carbonyl cyanide 3-chlorophenylhydrazone), which inhibits the mitochondrial membrane potential and disrupts the H$^+$ gradient in mammalian cells (30). First, we measured the mitochondrial potential with TMRE (tetramethylrhodamine, ethyl ester perchlorate) dye. We found that mitochondria in control sperm showed strong TMRE staining, suggestive of a healthy membrane potential (*SI Appendix*, Fig. S5A). Brief CCCP treatment caused a near-complete loss of TMRE staining, confirming that it damages mitochondrial potential dramatically (*SI Appendix*, Fig. S5A). Pretreatment of CCCP nearly completely blocked TEA-induced pseudopod formation and Zn^{2+} exit from mitochondria, further demonstrating that the H$^+$ gradient is necessary for SLC-30A9–mediated Zn^{2+} transport (Fig. 5 A and B and *SI Appendix*, Fig. S5 *B* and *C*).

To further test how release of zinc from mitochondria activates sperm, we treated sperm with the membrane-permeable Zn^{2+} chelator TPEN or the membrane-impermeable zinc chelator EGTA (ethylene glycol-bis[2-aminoethylether]-*N,N,N',N'*-tetraacetic acid). Both TPEN and EGTA reduced Zn^{2+} levels of sperm extracellular space, and TPEN also decreased Zn^{2+} levels in sperm (Fig. 3 C and D and *SI Appendix*, Fig. S5D). Both chelators reduced sperm activation induced by TEA and ammonium chloride (Fig. 5 C and D), which resembled the phenotype of the *slc-30a9* mutant. It further confirms that zinc release from mitochondria is required for sperm activation by weak bases. To test if MO fusion is normal in the *slc-30a9* mutant, we visualized MOs with FM1-43 as shown before (6). MO fusion sites marked by FM1-43 were found adjacent to the plasma membrane of both control and mutant sperm (Fig. 5 *E* and *F* and *SI Appendix*, Fig. S6A), suggesting MO fusion is normal in the *slc-30a9* mutant.

To complement these in vitro experiments on *C. elegans* sperm, we used brood size as a measure for sperm activation in vivo. The brood size of *slc-30a9* hermaphrodites was reduced to about 4% of control worms, demonstrating that SLC-30A9 plays important roles in fertility (Fig. 5G). To more directly assess the in vivo sperm activity, we quantified the cross-progenies of a female worm (*fog-2*) crossed with *slc-30a9* males. This cross yielded 47% of the progeny compared with control crosses, suggesting that *slc-30a9* sperm are defective in vivo (Fig. 5G). We also quantified the cross-progenies of *slc-30a9* hermaphrodites and *him-5* males, and found greatly reduced progeny number, suggesting oocytes are defective in the *slc-30a9* mutant (Fig. 5G).

Mitochondrial Transport to Dendrites and Axons Is Impaired in the *slc-30a9* Mutant. To ask whether there are other mitochondrial phenotypes in the *slc-30a9* mutant, we examined the distribution of mitochondria in PVD dendrites. In the WT PVD, mitochondria were distributed along the dendrites through DRP-1–mediated fission and microtubule-based transport events (31, 32) (Fig. 6A). The number of mitochondria in dendrites was greatly reduced in the *slc-30a9* mutant, indicating that some aspects of mitochondrial fission and/or transport are blocked in the mutant (Fig. 6 *A* and *B*). We found similarly reduced mitochondria in both axons and dendrites in the motor neuron DA9 in the *slc-30a9* mutant, further suggesting that SLC-30A9 is required for proper transport of mitochondria in neurites (Fig. 6 *D* and *E*).
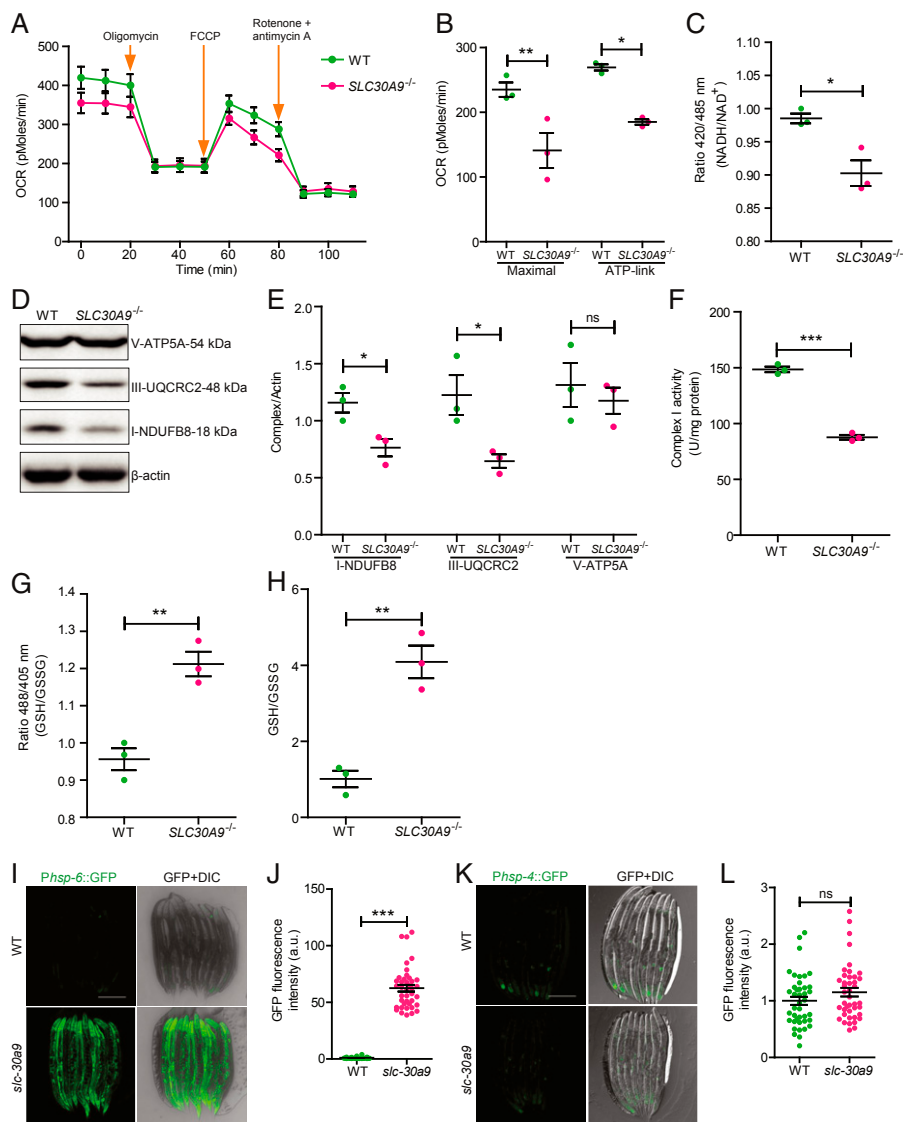
Fig. 4. SLC-30A9 is required for mitochondrial function. (*A*) The OCRs of WT and *SLC30A9*$^{-/-}$ were measured using a Seahorse XF24 analyzer under basal conditions and in response to 1.5 mM oligomycin (a complex V inhibitor), 4 mM FCCP (an uncoupler), or 2 mM rotenone (a complex I inhibitor) together with antimycin A. (*B*) ATP-linked OCR and maximal respiration capacity are plotted. Data are shown as mean ± SEM (*n* = 3). One-way ANOVA with Tukey correction. *$P < 0.05$, **$P < 0.01$. (*C*) The mitochondrial NADH/NAD$^+$ in WT and *SLC30A9*$^{-/-}$ cells was measured with the Mito-SoNar probe. Mito-SoNar fluorescence was excited by 420- and 485-nm light. Emission at 535 nm was measured using a microplate reader. Ratios between 420 and 485 nm were plotted. Data are shown as mean ± SEM (*n* = 3). *$P < 0.05$ by unpaired *t* test. (*D* and *E*) *SLC30A9*$^{-/-}$ KO decreases the abundance of mitochondrial complexes I and III. The expression of the respiratory complexes (OXPHOS) in WT and *SLC30A9*$^{-/-}$ cells was examined using Western blot and normalized in *E*. The OXPHOS antibody contains five monoclonal antibodies, one each against Complex I subunit NDUFB8, Complex II subunit SDHB, Complex III subunit UQCRC2, Complex IV COX II, and ATP5A as an optimized premixed cocktail. Data are shown as mean ± SEM (*n* = 3). *$P < 0.05$ by unpaired *t* test. (*F*) Mitochondrial respiratory chain complex I activity in WT and *SLC30A9*$^{-/-}$ cells was determined using a Micro Mitochondrial Respiratory Chain Complex I Assay Kit. Mitochondrial complex I activity was expressed as U/mg protein. Data are shown as mean ± SEM (*n* = 3). ***$P < 0.001$ by unpaired *t* test. (*G*) Mitochondrial GSH/GSSG in WT and *SLC30A9*$^{-/-}$ cells was measured by the Mito-Grx1-roGFP2 probe. The fluorescence emission at 525 nm elicited by 405- or 488-nm light was measured by a microplate reader. The 405/488-nm ratio was plotted for WT and *SLC30A9*$^{-/-}$ cells. Data are shown as mean ± SEM (*n* = 3). **$P < 0.01$ by unpaired *t* test. (*H*) Mitochondrial GSH/GSSG in WT and *SLC30A9*$^{-/-}$ cells was measured by a GSH and GSSG assay kit. Data are shown as mean ± SEM (*n* = 3). **$P < 0.01$ by unpaired *t* test. (*I*) Representative confocal images of transgenic animals expressing an integrated transgene, P*hsp-6*::GFP, in the WT and *slc-30a9(wy50591)* mutant. (Scale bar, 200 μm.) (*J*) Quantification of GFP fluorescence intensity of the WT and *slc-30a9(wy50591)* mutant. Data are shown as mean ± SEM. ***$P < 0.001$ by unpaired *t* test. Thirty-four or more worms were analyzed for each genotype. (*K*) Representative confocal images of the UPRer marker P*hsp-4*::GFP in the WT and *slc-30a9(wy50591)* mutant. (Scale bar, 200 μm.) (*L*) Quantification of GFP fluorescence intensity of the WT and *slc-30a9(wy50591)* mutant. Data are shown as mean ± SEM. Not significant by unpaired *t* test. Forty or more worms were analyzed for each genotype.

Discussion

Several lines of evidence presented here argue strongly that SLC-30A9 functions as a conserved, putative Zn^{2+} transporter to export zinc from mitochondria. First, its homology to other established SLC-30/ZnT family members makes it likely that SLC-30A9 has Zn^{2+} transport activity. A recent study on the structure of

SLC-30A8/ZnT8 showed that metazoan SLC-30 family proteins share structure homology with the well-studied bacteria homolog YiiP (24). Second, our mutagenesis experiment showed that the putative Zn^{2+}/H$^+$ binding sites are critical for the function of SLC-30A9, further arguing that SLC-30A9 is a Zn^{2+} transporter. Third, SLC-30A9 is mainly localized to mitochondria in multiple

Deng et al.
SLC-30A9 is required for Zn^{2+} homeostasis, Zn^{2+} mobilization, and mitochondrial health

PNAS | 7 of 12
https://doi.org/10.1073/pnas.2023909118

cell types in worms and a human cell line. Fourth, in the absence of the function of *slc-30a9*, both worm and vertebrate mitochondria are overloaded with Zn^{2+} and become dramatically swollen.

Lastly, SLC-30A9 is required for Zn^{2+} extrusion from mitochondria, a necessary step during activation of *C. elegans* sperm. Together, these data are consistent with the notion that SLC-30A9
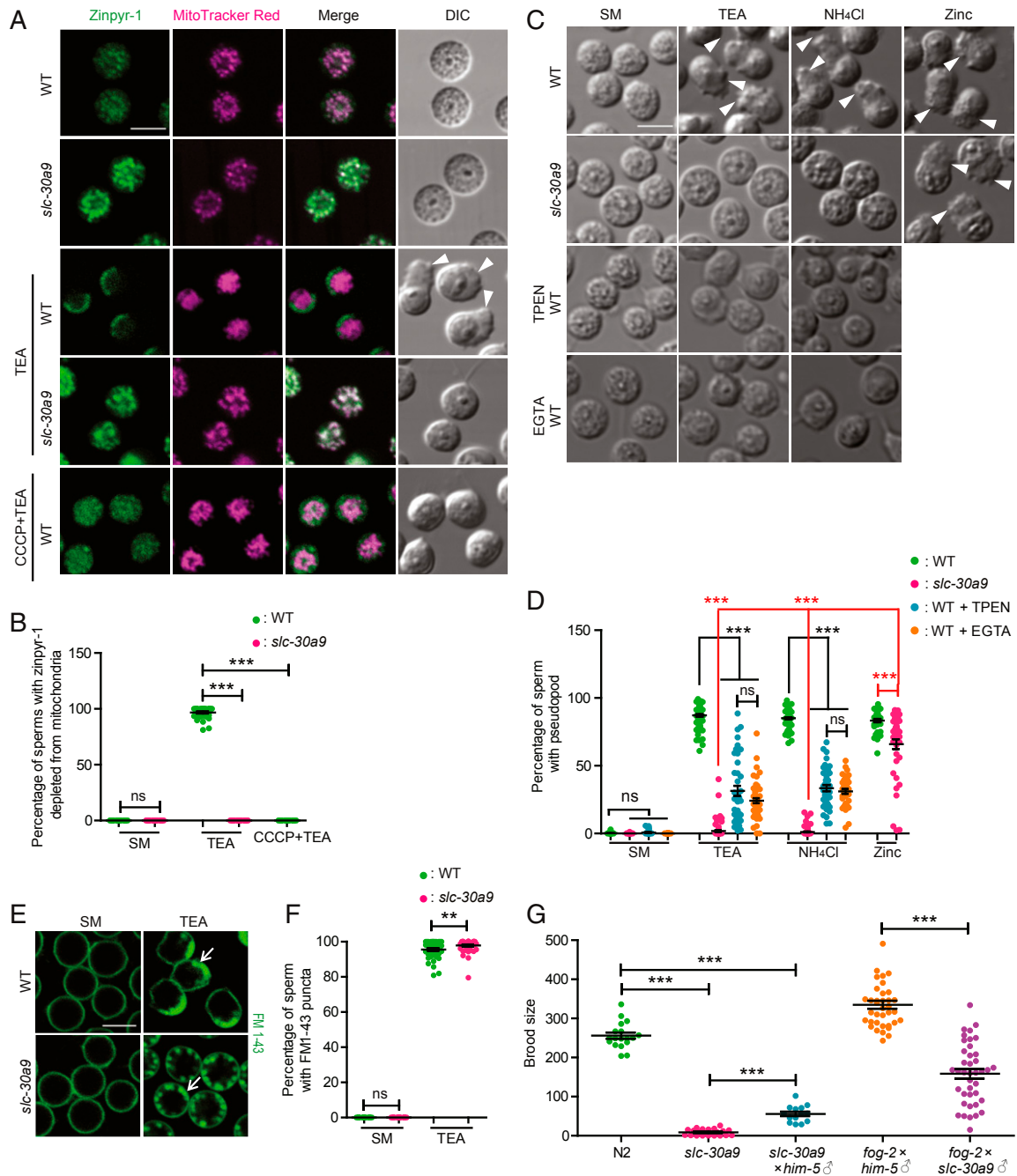
Fig. 5. SLC-30A9–mediated Zn^{2+} mobilization is required for sperm activation. (*A*) Representative confocal images of isolated spermatids costained with Zinpyr-1 green and MitoTracker red in *him-5(e1490)* and *slc-30a9(wy50591)*; *him-5(e1490)* mutant males treated with SM (control medium), SM + TEA, or SM + CCCP + TEA. The arrowheads indicate pseudopods. (Scale bar, 5 μm.) (*B*) Quantification of sperm with Zinpyr-1 depleted from mitochondria in *him-5(e1490)* and *slc-30a9(wy50591)*; *him-5(e1490)* mutants supplemented with SM, SM + TEA, or SM + CCCP + TEA. Data are shown as mean ± SEM. One-way ANOVA with Tukey correction. ***$P < 0.001$. Thirty-four worms or more were scored for each genotype. (*C*) DIC micrographs showing spermatids of *him-5(e1490)* and *slc-30a9(wy50591)*; *him-5(e1490)* in SM, SM + TPEN, and SM + EGTA stimulated by sperm activators TEA, NH_4Cl, or zinc in separate experiments. The arrowheads indicate pseudopods. (Scale bar, 5 μm.) (*D*) Quantification of sperm activation measured by pseudopods in *C*. Data are shown as mean ± SEM. One-way ANOVA with Tukey correction. ***$P < 0.001$. Forty or more worms were scored for each genotype. (*E*) Representative confocal images of spermatids stained with FM 1-43 in *him-5(e1490)* and *slc-30a9(wy50591)*; *him-5(e1490)* mutant males treated with SM or SM + TEA. The arrows indicate the putative MO fusion site at the rear edge of the spermatozoa. (Scale bar, 5 μm.) (*F*) Quantification of sperm with punctate FM 1-43 staining near the plasma membrane. Data are shown as mean ± SEM. One-way ANOVA with Tukey correction. **$P < 0.01$. Forty or more worms were scored for each genotype. (*G*) Quantification of total brood size of N2 hermaphrodites (*n* = 18), *slc-30a9(wy50591)* hermaphrodites (*n* = 22), cross-progenies between *him-5(e1490)* males and *slc-30a9(wy50591)* hermaphrodites (*n* = 14), cross-progenies between *him-5(e1490)* males and *fog-2(q71)* females (*n* = 37), and cross-progenies between *slc-30a9(wy50591)*; *him-5(e1490)* males and *fog-2(q71)* females (*n* = 40). Data are shown as mean ± SEM. One-way ANOVA with Tukey correction. ***$P < 0.001$.

exports Zn^{2+} from mitochondria in both invertebrate and vertebrate cells. Mitochondria are unique in that they contain a strong H^+ gradient which is maintained by the electron transport chain (ETC). It is plausible that this H^+ gradient provides the energy required for Zn^{2+} extrusion from mitochondria.

Perez and colleagues report that a SLC-30A9 mutation is responsible for one type of cerebrorenal syndrome (20). The subcellular localization experiments of SLC-30A9 in this paper have yielded inconclusive results. The authors did report a decreased cytosolic Zn^{2+} level in cells expressing mutant SLC-30A9, which is consistent with the notion that SLC-30A9 extrudes Zn^{2+} from the mitochondria into the cytosol. Cerebrorenal syndrome patients are characterized by intellectual disability and pronounced motor deficits. While the exact mechanisms underlying these deficits remain elusive, the lack of mitochondria in axons and dendrites of *C. elegans* neurons provides a potential cell biological mechanism for neuronal dysfunction. Interestingly, mitochondrial transport deficits in PVD neurons did not affect the morphogenesis of PVD neurons but instead led to degeneration of dendrites after development (32). This echoes a key feature of cerebrorenal syndrome patients who achieve major neural developmental landmarks but regress later (20). Together, we propose Zn^{2+} overload, mitochondrial swelling, and transport defect as potential cell biological mechanisms for cerebrorenal syndrome.

What is the physiological importance of maintaining Zn^{2+} in mitochondria? Our results shed light on two different aspects of SLC-30A9's function. First, at resting state, both invertebrate and vertebrate cells maintain a low level of Zn^{2+} to prevent mitochondrial swelling. In HeLa cells, loss of SLC30A9 causes reduced oxidative phosphorylation and reduced oxygen consumption rate. Several components of the mitochondrial respiratory complexes were reduced in levels, which may contribute to the partially blocked oxidative phosphorylation. Accordingly, this mitochondrial inactivity correlates with the elevated ratio of GSH/GSSG in the *SLC30A9*$^{-/-}$ cells. It has been shown that up-regulation of mitochondrial ETC complexes and OXPHOS causes a low GSH/GSSG ratio (33). The direct link between Zn^{2+} overloading and the physiological defects is unknown. However, given the dramatic swelling and markedly reduced cristae, it is plausible that multiple aspects of mitochondrial cell biology are affected such as import of proteins from the cytosol and organization of the inner membrane.

Second, in addition to maintaining the steady-state Zn^{2+} levels, SLC-30A9 also mobilizes Zn^{2+} during sperm activation. Zn^{2+} is required for fertility in many species. In sea urchins, extracellular zinc is reported to be essential for sperm motility and the acrosome reaction (15). Zinc shows four distinct subcellular localization patterns during mammalian sperm capacitation, suggestive of active Zn^{2+} mobilization (16). A previous study showed that Zn^{2+} redistributes from MOs to the extracellular space during sperm activation in *C. elegans* (6). Our results show that mobilization of Zn^{2+} from mitochondria through SLC-30A9 is required for activation of sperm in vitro by weak bases. In vivo, SLC-30A9 is required for normal brood size, further supporting a physiological role in sperm activation.

In summary, we identified SLC-30A9 as a putative mitochondrial Zn^{2+} transporter to export Zn^{2+} from mitochondria. This function is required for maintaining Zn^{2+} homeostasis and preventing mitochondrial swelling in the resting state. We also show that SLC-30A9 is required for Zn^{2+} mobilization during sperm activation, suggesting it is required for dynamic regulation of Zn^{2+} concentration for its signaling function. Lastly, based on the mitochondrial distribution defects in worm neurons, we propose that mitochondrial swelling and transport defects in neurons might underlie one form of cerebrorenal syndrome.

Materials and Methods

***C. elegans* Strains.** *C. elegans* strains used in this study were cultured at 20 °C on nematode growth medium (NGM) plates seeded with *Escherichia coli* OP50 using standard methods (34). N2 is the standard strain and all the mutants were isolated from N2.

Constructs and Transgenes. Phusion DNA polymerase (New England Biolabs) or TransStart FastPfu DNA polymerase (TransGen Biotech) was used to amplify PCR products by standard procedures. The Clontech In-Fusion PCR Cloning System was used to construct plasmids (35). Transgenic worms were generated by injection using standard methods (36). P*odr-1*::GFP or P*myo-2*::mCherry was used as the coinjection marker.
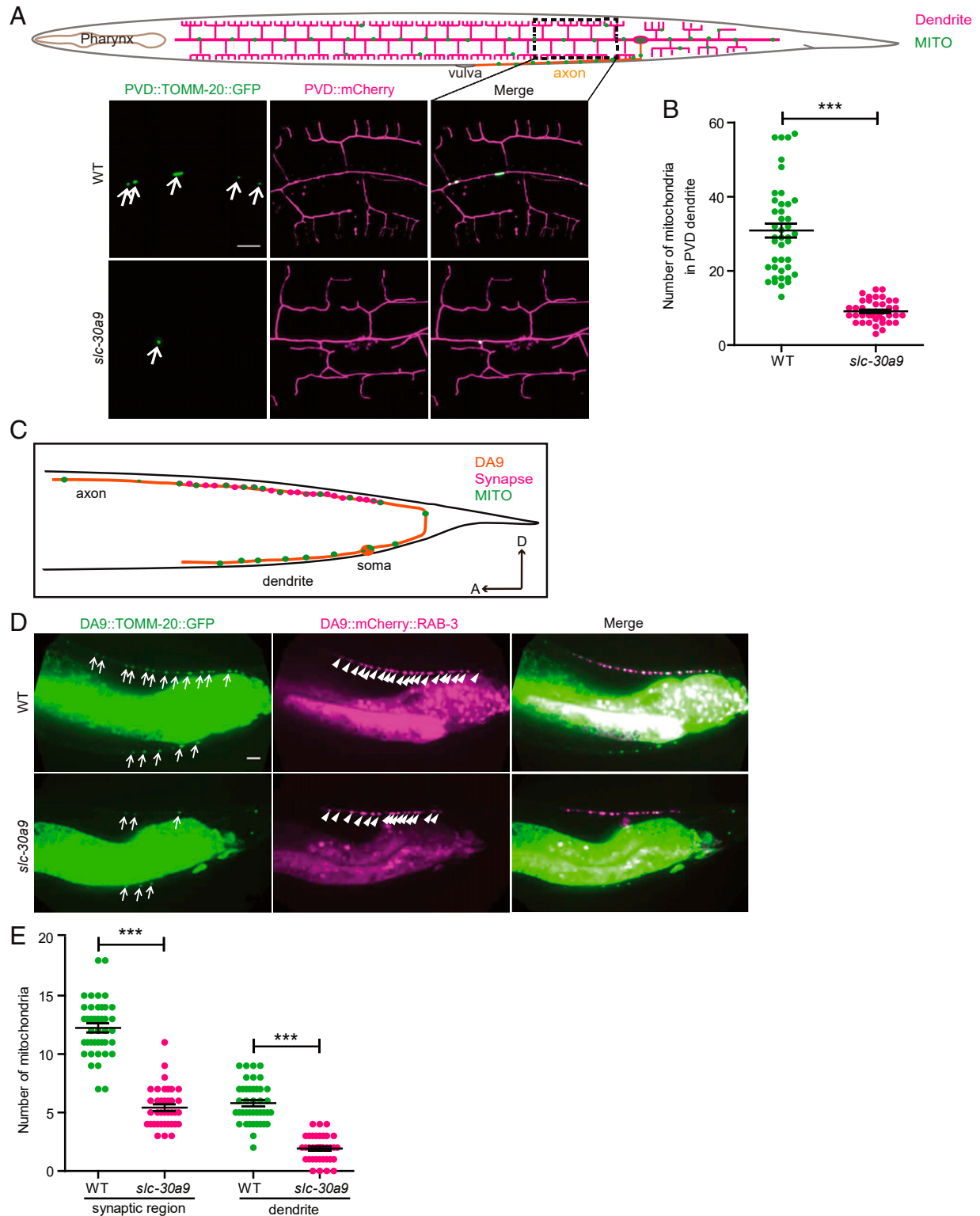
Microscope System. Young adult worms were anesthetized with 0.1 mmol/L levamisole in M9 buffer and mounted on 3% agarose pads. Imaging was performed on an Olympus FV1200 confocal microscope with a 60×/1.35 numerical aperture objective, spinning disk confocal (Yokogawa; CSU-X1 Spinning Disk Unit) with a 100×/1.4 numerical aperture objective, 488 nm and 561 nm lasers, and a zeiss LSM 980 confocal microscope with a 60×/1.4 numerical aperture objectivem, 458 nm and 508 nm lasers (35).

Three-dimensional SIM images of worms were acquired on the DeltaVision OMX V3 Imaging System (GE Healthcare) with a 100×/1.40 numerical aperture oil objective (Olympus; UPlanSApo), solid-state multimode lasers (488 and 561 nm), and electron-multiplying charge-coupled device cameras (Evolve; 256 × 256; Photometrics). Serial *Z* stack sectioning was done at 125-nm intervals for SIM mode. To obtain optimal images, immersion oils with refractive indices of 1.520 were used for worms on glass coverslips. The microscope is routinely calibrated with 100-nm fluorescent spheres to calculate both the lateral and axial limits of image resolution. SIM image stacks were reconstructed using softWoRx 6.1.1 (GE Healthcare) with the following settings: pixel size 39.5 nm; channel-specific optical transfer functions; Wiener filter constant 0.0010; discard negative intensities background; drift correction with respect to first angle; and custom K0 guess angles for camera positions. The reconstructed images were further processed for maximum-intensity projections with softWoRx 6.1.1. Pixel registration was corrected to be less than 1 pixel for all channels using 100-nm TetraSpeck beads.

Electron Microscopy. Briefly, in the high-pressure freeze (HPF) procedure, several living worms were picked into a type A specimen carrier (200-μm well) containing 10% bovine serum albumin (BSA) to avoid voids and overfilling. Then they were placed in a treated type B carrier (flat) with hexadecane and closed before freezing in the HPF device (Leica; HPM100). Following the HPF procedure, the fast-frozen samples were immersed in a freezing tube containing 2% osmium tetroxide in 98% acetone, 2% water and placed into the freeze substitution (FS) device (Leica; EM AFS) set to the following parameters: T1 −90 °C for 72 h, S1 5 °C/h, T2 −60 °C for 12 h, S2 5 °C/h, T3 −30 °C for 10 h, and then slowly warmed to 10 °C (5 °C/h). Following FS, samples were rinsed four times in 100% acetone, 15 min each, at room temperature (RT). Next, they were stained in 1% uranyl acetate dissolved in 90% acetone, 10% methanol (filtered before use) for 2 h in the dark at RT. After staining, samples were rinsed four times in 100% acetone, 15 min each, at RT, and then transferred into new 2-mL Eppendorf tubes. After that, they were infiltrated in graded mixtures (1:3, 1:1, 1:3) of resin (EMS; resin mixture: 16.2 mL SPI-PON812, 10 mL dodecenyl succinic anhydride [DDSA], 8.9 mL nadic methyl anhydride [NMA], 1.5% N,N-Dimethylbenzylamine [BDMA]) and acetone mixture, and then changed into 100% resin, which was replaced three times over the next 2 d on a rotator. Finally, worms were embedded and polymerized for 12 h at 45 °C and 48 h at 60 °C. The ultrathin sections (70 nm) were sectioned with a microtome (Leica; EM UC6) and imaged on a transmission electron microscope (FEI; Tecnai Spirit 120 kV).

Cells were fixed with 2.5% (volume [vol]/vol) glutaraldehyde with phosphate buffer (PB) (0.1 M, pH 7.4), and washed four times in PB at 4 °C. Then cells were fixed with 1% (weight [wt]/vol) OsO₄ and 1.5% (wt/vol) potassium ferricyanide aqueous solution at 4 °C for 2 h, and dehydrated through a graded ethanol series (30, 50, 70, 80, 90, 100%, 100%, 5 min each at 4 °C) into pure acetone (2 × 5 min). Samples were infiltrated in graded mixtures (3:1, 1:1, 1:3) of acetone and SPI-PON812 resin (16.2 mL SPI-PON812, 10 mL DDSA, 8.9 mL NMA) and then changed to pure resin. Finally, cells were embedded in pure resin with 1.5% BDMA and polymerized for 12 h at 45 °C and 48 h at 60 °C. The ultrathin sections (70 nm thick) were sectioned with a microtome (Leica; EM UC7), double-stained by uranyl acetate and lead citrate, and examined by a transmission electron microscope (FEI; Tecnai Spirit 120 kV).

In Vitro Sperm Activation. Virgin L4 males were placed on NGM plates for 48 to 72 h at 20 °C. The spermatids were dissected and released into a drop of sperm medium (SM) buffer (50 mM Hepes, 45 mM NaCl, 25 mM KCl, 1 mM MgCl₂, 5 mM CaCl₂, 10 mg/mL polyvinylpyrrolidone, pH 7.0). These sperm

Deng et al.
SLC-30A9 is required for Zn²⁺ homeostasis, Zn²⁺ mobilization, and mitochondrial health

PNAS | 9 of 12
https://doi.org/10.1073/pnas.2023909118

CELL BIOLOGY

Fig. 6. Mitochondrial transportation to dendrites and axons is impaired in the *slc-30a9* mutant. (*A*) Schematic drawing of PVD neurites and the mitochondrial pattern. Representative confocal images of a PVD cell expressing TOMM-20(1-54AA)::GFP and PVD::mCherry in the WT and *slc-30a9(wy50591)* mutant. The arrows indicate mitochondria. (Scale bar, 10 μm.) (*B*) Quantification of mitochondrial number in PVD dendrites of the WT and *slc-30a9(wy50591)* mutant. Data are shown as mean ± SEM. ***$P < 0.001$ by unpaired t test. Forty or more worms were analyzed for each genotype. (*C*) Schematic drawing of the DA9 synapse and mitochondrial pattern. (*D*) Representative confocal images of a DA9 cell expressing TOMM-20(1-54AA)::GFP and mCherry::RAB-3, illustrating synapses, in the WT and *slc-30a9(wy50591)* mutant. The arrows indicate mitochondria, and the arrowheads show synapses. (Scale bar, 10 μm.) (*E*) Quantification of mitochondrial number in DA9 dendrites and the synaptic region of the WT and *slc-30a9(wy50591)* mutant. Data are shown as mean ± SEM. One-way ANOVA with Tukey correction. ***$P < 0.001$. Forty worms or more were scored for each genotype.

were maintained in a chamber constructed by mounting a 22 × 30-mm glass coverslip onto a glass slide over parallel strips of two-sided sticky tape. Then, 30 mM TEA, 40 mM NH$_4$Cl, or 2 mM ZnCl$_2$ was added into the chamber and incubated for 7 to 10 min to activate the sperm. In the chelating zinc assay, spermatids were incubated with 400 µM TPEN (Sigma; P4413) or 10 mM EGTA (Sigma; E4378) in SM buffer for 10 min at RT. Then, 30 mM TEA, 40 mM NH$_4$Cl with 400 µM TPEN, or 10 mM EGTA was added to the chamber and incubated for 7 to 10 min to activate the sperm. The images were captured using an FV1200 confocal microscope.

Zinpyr-1 and MitoTracker Fluorescent Imaging. Spermatids were incubated with 10 µM Zinpyr-1 (Cayman; 15122) and 1 µM MitoTracker red (Invitrogen; M7512) in divalent calcium-free SM buffer for 10 min at RT. In the chelating assay, spermatids were incubated with 400 µM TPEN or 10 mM EGTA in calcium-free SM buffer for 10 min. Then sperm were washed with 10 µM Zinpyr-1, 1 µM MitoTracker red, 400 µM TPEN, or 10 mM EGTA in divalent calcium-free SM buffer for 10 min at RT. The fluorescent images were captured using an FV1200 confocal microscope.

TMRE Fluorescent Imaging. Spermatids were incubated with 10 µM CCCP (MCE; HY-100941) in SM buffer for 10 min at RT. Then sperm were washed with 10 µM CCCP, 100 nM TMRE (Thermo Fisher Scientific; T669) in SM buffer for 10 min. The fluorescent images were captured using an FV1200 confocal microscope.

MO Fusion Assay. An MO fusion assay was performed as described previously (37). Briefly, spermatids or spermatozoa were perfused with FM 1-43 (Invitrogen; F35355) in SM buffer at 5 µg/mL for 3 min to visualize the plasma membrane and fused MOs using an FV1200 confocal microscope.

Fertility Assays. To measure hermaphrodite fertility, we placed individual L4 animals on freshly seeded dishes, transferred them to new dishes every 8 to 16 h for 5 d, and scored the number of fertilized eggs and unfertilized oocytes on each dish. To measure *C. elegans* male fertility, individual males were crossed to individual *fog-2(q71)* L4 hermaphrodites for 24 h. The male was removed, the hermaphrodite was transferred to a new dish every 24 h, and then the offspring were scored at adulthood.

ZapCY1 FRET. An acceptor photobleaching analysis method was used to measure PVD::mito-ZapCY1 and PVD::ER-ZapCY1 FRET efficiency, and dequenching of the donor after selective photobleaching of the acceptor causes an increase in donor emission that can be quantified. FRET efficiency = ((Dpost − Dpre)/Dpost) × 100. The fluorescent images were captured using an FV1000 confocal microscope (38).

Cell Culture. HeLa cells (ATCC) were cultured in high-glucose Dulbecco's modified Eagle's medium containing 10% fetal bovine serum (Gibco) and 100 µg/mL penicillin-streptomycin at 37 °C in 5% CO$_2$. No mycoplasma contamination was observed during cell culture.

SLC30A9 Gene Knockout Using the CRISPR-Cas9 System. The CRISPR-Cas9 system was used to disrupt the expression of the *SLC30A9* gene. In brief, a single-guide RNA (sgRNA) sequence was selected using an optimized CRISPR design. The sgRNA sequence for *SLC30A9* was 5′-CCCTGTAGTCATCCATATATTGG-3′, corresponding to exon 2. AAV-U6-sgRNA-CMV-mCherry–expressing sgRNA was expressed in the HeLa cell line stably expressing Cas9 protein. To establish a knockout clone, the cells expressing mCherry were sorted using fluorescence-activated cell sorting (BD FACSAria™ IIIu). A single clone was selected, expanded, and then used for biological assays. For sequence analysis of the *SLC30A9* gene, the following primer set was used: forward, 5′-AAAATCGGTGACAGT-ATGAATGAAT-3′ and reverse, 5′-TAATAAAACACAA ACCTCTGGGAAG-3′. AAV-U6-sgRNA-CMV-mCherry was a gift from Wensheng Wei, Peking University, Beijing, China.

Redox States in Mitochondrion Detection. Mitochondrion redox states in cells were detected by redox probes. WT and *SLC30A9*$^{-/-}$ cells were transduced with lentiviruses expressing redox probes and detected with a microplate reader. Mito-Grx1-roGFP2–sensing GSH and GSSG, ratio 488/405 nm, indicates the level of GSH/GSSG. Mito-SoNar–sensing NADH and NAD$^+$, ratio 420/485 nm, indicates the level of NADH/NAD$^+$.

Zinpyr-1 and MitoTracker Fluorescent Imaging of HeLa Cells. Zinpyr-1 is a fluorescein-based bright fluorescent sensor for divalent zinc. HeLa cells were incubated with 20 µM Zinpyr-1 (ChemCruz; sc-213182) and 10 µM Mito 405 (Biotium; 70070-T) in

divalent calcium-free, magnesium-free Hanks' balanced salt saline (HBSS; 14170-112; Gibco) at 37 °C, 5% CO$_2$ for 20 min, and then washed out and replaced with fresh HBSS. A Carl Zeiss LSM 710 confocal microscope equipped with a 63× oil-immersion objective was used to obtain fluorescence microscopy images.

Immunofluorescent Staining. WT and *SLC30A9*$^{-/-}$ cells expressing mito-BFP were fixed with 4% paraformaldehyde at RT for 20 min and permeabilized with 0.1% Triton X-100 in phosphate-buffered saline (PBS) for 5 min at room temperature. After incubation with 1% BSA at room temperature for 1 h, the cells were incubated with SLC30A9 antibodies at 4 °C overnight. Subsequently, the cells were incubated with secondary antibodies at RT for 1 h. A Zeiss LSM 710 confocal microscope was used for imaging.

Western Blot. Cells were lysed in radio immunoprecipitation assay buffer with a protease inhibitor mixture solution (Roche). The protein concentration was measured by the BCA Kit, and 5× sodium dodecyl sulfate-polyacrylamide gel electrophoresis (SDS-PAGE) reducing loading buffer was added to each sample and boiled at 100 °C for 10 min. Approximately 20 mg of protein was subjected to SDS-PAGE and electrotransferred to a polyvinylidene fluoride membrane (Millipore). The membranes were blocked in 5% milk and then incubated with primary antibodies and horseradish peroxidase–conjugated secondary antibodies (1:2,000; Sungene Biotech). The quantification of Western blotting was performed with Image Lab software for the ChemiDoc XRS System (Bio-Rad).

qPCR. The RNA from whole-cell pellets was extracted with TRIzol reagent (Invitrogen) according to the manufacturer's instructions, followed by complementary DNA synthesis with the Moloney Murine Leukemia Virus Reverse Transcriptase System (Promega). qRT-PCR was performed with the qPCR Mix in Real-Time PCR System (Applied Biosystems) using real-time PCR Master Mix (SYBR Green), and β-actin was used as the reference gene.

Oxygen Consumption Measurement. Mitochondrial metabolic levels can be determined by conducting oxygen consumption measurement. OCRs of HeLa cells (WT and *SLC30A9*$^{-/-}$) were measured using a Seahorse XF24 extracellular flux analyzer (Seahorse Bioscience). HeLa cells were seeded at 5×10^4 per well in 24-well XF plates. Hydrated liquid (525 µL) was added to each well of a Seahorse XF24 cell-culture plate and incubated overnight at RT. OCR testing was done according to the manufacturer.

Mitochondrial Respiratory Chain Complex I Activity Detection. The complex I activity in cells was determined using a Micro Mitochondrial Respiratory Chain Complex I Assay Kit (Solarbio). Briefly, complex I (EC 1.6.5.3), also known as NADH CoQ reductase or NADH dehydrogenase, catalyzes the transfer of a pair of electrons from NADH to CoQ and reduces O$_2$ to O^{2-}, which is the main part of the respiratory electron transport chain. Complex I can catalyze the dehydrogenation of NADH to NAD$^+$. The oxidation rate of NADH was measured at 340 nm, and the activity of complex I was calculated; 1 U was defined as the consumption of 1 nmol NADH/min. Mitochondrial complex I activity was expressed as U/mg protein.

Detection of GSH/GSSG in Mitochondria. Isolation of mitochondria from HeLa cells was performed as described (39). In brief, HeLa cells grown to 90% confluency on a 10-cm plate were washed three times by PBS buffer before being digested by trypsin. Then the cells were washed three times by PBS buffer by centrifugation at $1,100 \times g$ for 3 min at 4 °C, before being washed three times by PBS buffer. The cells were resuspended in 1 mL ice-cold isolation buffer with protease inhibitor mixture. The mixture was transferred to a 1.5-mL ice-cold tube, before being homogenized by a 2-mL syringe. The homogenate was centrifuged at $600 \times g$ for 10 min at 4 °C. The supernatant was transferred to a new ice-cold tube for centrifugation at $14,000 \times g$ for 15 min at 4 °C. The pellet was washed three times by PBS buffer. The measurement of mitochondrial protein concentration was performed by the BCA method, and GSH/GSSG detection was performed by a GSH and GSSG detection kit (Beyotime; S0053).

Quantification. Data were analyzed with GraphPad Prism software to generate graphs. Error bars represent SEM. The two-tailed unpaired *t* test was used for statistical analysis of two groups of samples. One-way ANOVA with Tukey correction was used to compare the mean differences between multiple groups. For all quantifications, *$P < 0.05$, **$P < 0.01$, and ***$P < 0.001$; ns indicates not significant.

Deng et al.
SLC-30A9 is required for Zn^{2+} homeostasis, Zn^{2+} mobilization, and mitochondrial health

PNAS | 11 of 12
https://doi.org/10.1073/pnas.2023909118

1. T. Kambe, T. Tsuji, A. Hashimoto, N. Itsumura, The physiological, biochemical, and molecular roles of zinc transporters in zinc homeostasis and metabolism. *Physiol. Rev.* **95**, 749–784 (2015).
2. M Hambidge, Human zinc deficiency. *J. Nutr.* **130**, 1344S–1349S (2000).
3. K. Tóth, Zinc in neurotransmission. *Annu. Rev. Nutr.* **31**, 139–153 (2011).
4. S. Yamasaki *et al.*, Zinc is a novel intracellular second messenger. *J. Cell Biol.* **177**, 637–645 (2007).
5. D. J. Eide, Zinc transporters and the cellular trafficking of zinc. *Biochim. Biophys. Acta* **1763**, 711–722 (2006).
6. Z. Liu, L. Chen, Y. Shang, P. Huang, L. Miao, The micronutrient element zinc modulates sperm activation through the SPE-8 pathway in *Caenorhabditis elegans*. *Development* **140**, 2103–2107 (2013).
7. J. Jeong, D. J. Eide, The SLC39 family of zinc transporters. *Mol. Aspects Med.* **34**, 612–619 (2013).
8. Y. H. Kim, J. W. Eom, J. Y. Koh, Mechanism of zinc excitotoxicity: A focus on AMPK. *Front. Neurosci.* **14**, 577958 (2020).
9. S. L. Sensi, P. Paoletti, A. I. Bush, I. Sekler, Zinc in the physiology and pathology of the CNS. *Nat. Rev. Neurosci.* **10**, 780–791 (2009).
10. B. Besecker *et al.*, The human zinc transporter SLC39A8 (Zip8) is critical in zinc-mediated cytoprotection in lung epithelia. *Am. J. Physiol. Lung Cell. Mol. Physiol.* **294**, L1127–L1136 (2008).
11. S. G. Ji, Y. V. Medvedeva, J. H. Weiss, Zn^{2+} entry through the mitochondrial calcium uniporter is a critical contributor to mitochondrial dysfunction and neurodegeneration. *Exp. Neurol.* **325**, 113161 (2020).
12. D. Jiang, P. G. Sullivan, S. L. Sensi, O. Steward, J. H. Weiss, Zn(2+) induces permeability transition pore opening and release of pro-apoptotic peptides from neuronal mitochondria. *J. Biol. Chem.* **276**, 47524–47529 (2001).
13. L. M. Malaiyandi, O. Vergun, K. E. Dineley, I. J. Reynolds, Direct visualization of mitochondrial zinc accumulation reveals uniporter-dependent and -independent transport mechanisms. *J. Neurochem.* **93**, 1242–1250 (2005).
14. M. B. Sørensen *et al.*, Zinc, magnesium and calcium in human seminal fluid: Relations to other semen parameters and fertility. *Mol. Hum. Reprod.* **5**, 331–337 (1999).
15. D. L. Clapper, J. A. Davis, P. J. Lamothe, D. Patton, D. Epel, Involvement of zinc in the regulation of pHi, motility, and acrosome reactions in sea urchin sperm. *J. Cell Biol.* **100**, 1817–1824 (1985).
16. K. Kerns, M. Zigo, E. Z. Drobnis, M. Sutovsky, P. Sutovsky, Zinc ion flux during mammalian sperm capacitation. *Nat. Commun.* **9**, 2061 (2018).
17. X. Ma, Y. Zhao, W. Sun, K. Shimabukuro, L. Miao, Transformation: How do nematode sperm become activated and crawl? *Protein Cell* **3**, 755–761 (2012).
18. H. Nishimura, S. W. L'Hernault, Spermatogenesis. *Curr. Biol.* **27**, R988–R994 (2017).
19. Y. Zhao *et al.*, The zinc transporter ZIPT-7.1 regulates sperm activation in nematodes. *PLoS Biol.* **16**, e2005069 (2018).
20. Y. Perez *et al.*, SLC30A9 mutation affecting intracellular zinc homeostasis causes a novel cerebro-renal syndrome. *Brain* **140**, 928–939 (2017).
21. M. Lu, D. Fu, Structure of the zinc transporter YiiP. *Science* **317**, 1746–1748 (2007).
22. E. Ohana *et al.*, Identification of the Zn^{2+} binding site and mode of operation of a mammalian Zn^{2+} transporter. *J. Biol. Chem.* **284**, 17677–17686 (2009).
23. Y. Golan, R. Alhadeff, A. Warshel, Y. G. Assaraf, ZnT2 is an electroneutral proton-coupled vesicular antiporter displaying an apparent stoichiometry of two protons per zinc ion. *PLoS Comput. Biol.* **15**, e1006882 (2019).
24. J. Xue, T. Xie, W. Zeng, Y. Jiang, X. C. Bai, Cryo-EM structures of human ZnT8 in both outward- and inward-facing conformations. *eLife* **9**, e58823 (2020).
25. Y. Qin, P. J. Dittmer, J. G. Park, K. B. Jansen, A. E. Palmer, Measuring steady-state and dynamic endoplasmic reticulum and Golgi Zn^{2+} with genetically encoded sensors. *Proc. Natl. Acad. Sci. U.S.A.* **108**, 7351–7356 (2011).
26. Q. Lu, H. Haragopal, K. G. Slepchenko, C. Stork, Y. V. Li, Intracellular zinc distribution in mitochondria, ER and the Golgi apparatus. *Int. J. Physiol. Pathophysiol. Pharmacol.* **8**, 35–43 (2016).
27. J. Zhang, Q. Zhang, Using Seahorse machine to measure OCR and ECAR in cancer cells. *Methods Mol. Biol.* **1928**, 353–363 (2019).
28. Y. Zhao *et al.*, SoNar, a highly responsive NAD^+/NADH sensor, allows high-throughput metabolic screening of anti-tumor agents. *Cell Metab.* **21**, 777–789 (2015).
29. M. Gutscher *et al.*, Real-time imaging of the intracellular glutathione redox potential. *Nat. Methods* **5**, 553–559 (2008).
30. Y. Q. Zhang *et al.*, Mitochondrial uncoupler carbonyl cyanide *m*-chlorophenylhydrazone induces vasorelaxation without involving K_{ATP} channel activation in smooth muscle cells of arteries. *Br. J. Pharmacol.* **173**, 3145–3158 (2016).
31. X. Liu *et al.*, Atlastin-1 regulates morphology and function of endoplasmic reticulum in dendrites. *Nat. Commun.* **10**, 568 (2019).
32. Y. Zhao *et al.*, Metaxins are core components of mitochondrial transport adaptor complexes. *Nat. Commun.* **12**, 83 (2021).
33. V. Costiniti *et al.*, Mitochondrial function in enamel development. *Front. Physiol.* **11**, 538 (2020).
34. S. Brenner, The genetics of *Caenorhabditis elegans*. *Genetics* **77**, 71–94 (1974).
35. Y. Chai *et al.*, Live imaging of cellular dynamics during *Caenorhabditis elegans* postembryonic development. *Nat. Protoc.* **7**, 2090–2102 (2012).
36. D. T. Stinchcomb, J. E. Shaw, S. H. Carr, D. Hirsh, Extrachromosomal DNA transformation of *Caenorhabditis elegans*. *Mol. Cell. Biol.* **5**, 3484–3496 (1985).
37. N. L. Washington, S. Ward, FER-1 regulates Ca^{2+}-mediated membrane fusion during *C. elegans* spermatogenesis. *J. Cell Sci.* **119**, 2552–2562 (2006).
38. T. Karpova, J. G. McNally, Detecting protein-protein interactions with CFP-YFP FRET by acceptor photobleaching. *Curr. Protoc. Cytom.* **35**, 12.7 (2006).
39. P. Jha, X. Wang, J. Auwerx, Analysis of mitochondrial respiratory chain supercomplexes using blue native polyacrylamide gel electrophoresis (BN-PAGE). *Curr. Protoc. Mouse Biol.* **6**, 1–14 (2016).